A Detector-Response Compensation Simulation Study With 3D MLEM in SPECT Compares Distance-Dependent and Distance-Nondependent Resolution Methods

Nuha Altubaynawi[1,2], Boubaker Zarrad[1], Mohammed Aida[1]

[1]Department of Physics, Faculty of Science, King Abdulaziz University, Jeddah, Saudi Arabia
[2]Department of physics, Faculty of Science, Hail University, Hail, Saudi Arabia

Abstract

Background

Correcting spatial resolution in single photon emission computed tomography (SPECT) using iterative methods has proven effective in many studies. This correction involves using a projection matrix (projector) to simulate the acquisition of projections by a gamma camera, along with a back-projection matrix (back-projector), which is generally the transpose of the projector without any attenuation modeling. This study examined the contribution of distance-dependent detector-response compensation (DRC) and compared it to the accelerated version and the distance-nondependent method. Two projectors (P1 and P2) and their corresponding back-projectors (B1 and B2) were implemented. P1 represented the distance-dependent response model, while P2 represented a nondependent average response model. Three reconstruction pairs were used: P1/B1 and P1/B2 for distance-dependent DRC, and P2/B2 for distance-nondependent DRC. The reconstruction method was the full 3D maximum-likelihood expectation maximization (MLEM), using simulated digital phantom projections that included attenuation, distance-dependent resolution, and Poisson noise without considering scatter.

Results

The assessment used transaxial slices. For full-width at half maximum (FWHM) spatial resolution, P1 outperformed P2. P1/B2 outperformed P1/B1, while getting closer after each iteration. Regarding Poisson noise, P1/B1 was more efficient than P1/B2 and P2/B2. Edge artifacts and overshoots were less intense with P2/B2 than the other pairs. P1/B2 and P2/B2 achieved the best relative contrast performance. The root mean squared error (RMSE) or normalized mean error (NME) showed that P1/B1 was best for low projection counts and large iteration numbers, while P1/B2 was best for high projection counts and low iteration numbers. On RMSE, the reconstruction pair performance depended on projection noise level, phantom insert size and type, and iteration.

Conclusions

No pair was consistently more efficient than the others across all parameters. Using P1/B1, which is far from convergence iteration, could yield results similar to other methods. Considering scatter would likely result in worse and more similar results across the three pairs. Although P2/B2 generally performed worse than P1/B2, they were similar and had more straightforward implementation. The number of iterations should be chosen according to the reconstruction pair, projection count, and desired spatial resolution.

Keywords

Detector-response compensation, SPECT, MLEM, Image quality assessment.

Background

Single photon emission computed tomography (SPECT) images are used for qualitative assessments of diseases pre- and postintervention and individualized dosimetry for planning and monitoring therapies that use internally applied radionuclides.[1-3] Unfortunately, attenuation, detector response, and scattering degrade SPECT's qualitative and quantitative accuracy. The collimator-detector system's limited resolution partly causes the reconstructed images' poor resolution.[4] A central limitation of nuclear medicine imaging is its relatively low spatial resolution that accentuates the partial volume effects, leading to a notable radioactivity concentration underestimation in volumes ~2–3 times less than the spatial resolution of the imaging system.[5]

In SPECT, the detector response is the convolution product of the gamma camera's intrinsic and collimator's responses. The latter depends on the distance between the source and the detector.[6] The detector point spread function (PSF) can be expressed by a two-dimensional Gaussian whose

full width at half maximum (FWHM) increases linearly with the distance between the gamma source and the detector.[7] PSF describes the acquisition of primary photons with a parallel hole collimator. This distance-dependent resolution in the acquired projections leads to a non-stationary blurring of the reconstructed images.[8]

In nuclear medicine, iterative methods for reconstructing SPECT data are widely used and allow qualitative and quantitative improvement of reconstructed transaxial slices by mathematically modeling the projection acquisition process. Which allows the correction of the attenuation and the detector response. Scattering correction is a more complex problem, and scatter compensation methods based on estimating the scatter component in the photo-peak projection—like Jaszczak's dual energy window, triple energy window, or the effective scatter source estimation methods—are the most popular.[9]

Two methods have been proposed for detector-response compensation (DRC): analytical methods using restoration filtering [10-13] and iterative methods using mathematical modeling of the acquisition process.[14-18] For iterative methods, a distance-dependent response model is incorporated into an iterative reconstruction algorithm. This requires repetition of the convolution product between the PSF and the reconstructed slices at each iteration. The slices reconstructed using these methods are more accurate but require a longer execution than analytical methods.[19] The resolution improves with each iteration, but the noise level increases. To remedy this, another approach has been proposed. It imposes a constant resolution by applying many iterations, followed by Gaussian post-reconstruction filtering (PRF). Hutton *et al.* found that using maximum-likelihood expectation maximization (MLEM)[20,21] and MCAT phantom, DRC alone yielded superior outcomes compared to the combination of PRF and DRC. The results suggest that using DRC without PRF and limiting the number of iterations could yield satisfactory results for myocardial SPECT.[22]

Compared to the 2D implementation of the quantitative compensation methods, the 3D implementation provides the most accurate SPECT image in terms of quantitative accuracy, spatial resolution, and noise; however, this method carries high computational requirements.[23]
We used the entirely 3D iterative MLEM technique with these pairings for tomographic reconstruction. We assumed that the scattering was completely rectified by the energy windowing approaches. The phantoms' geometry and composition allowed for nearly perfect attenuation correction. The projection operator P1 was used to create noise-free projections. P1, therefore, represents the ideal projection operator for the distance-dependent DRC. P1/B1 constitutes the optimal reconstruction pair.

The parameters utilized in the simulation were derived from those used in nuclear medicine to replicate real conditions. Image format: 128x128; pixel size: 4.5 mm; 360◦ SPECT with 120 projections; radius of rotation: 20 cm; FWHM varied from 7–15 mm for source-detector distance (dD) ranging from 10–30 cm;[19] and a total count per projection of $2\ 10^6$, 10^6, $5\ 10^5$, $2.5\ 10^5$, and 10^5. These counts cover both clinical and quality control applications.[24-26] The chosen radionuclide for this simulation (^{99m}Tc) is the most widely used in nuclear medicine.
We examined the limitations of the optimal compensation method and compared it to its accelerated or approximate versions. We used a personal computer (11th Gen Intel(R) Core(TM) i7-1195G7 2.90GHz) operating Windows 11 Home (Microsoft Corp.) and ImageJ software for image

display. 3D phantom generation, projection acquisition simulation, tomographic iterative reconstruction, and analyses were performed using an in-house application developed with Delphi 10.4. Computations were performed with single-precision floating-point arithmetic.

Methods

This section describes the digital phantom generation, the projection data simulation, resolution recovery, and assessment methods.

A. Phantom generation

The simulated phantoms used in this work comprised a superposition of spheres and cylinders of different sizes. Simple phantom shapes (spheres and cylinders) were chosen because of their suitability for evaluating SPECT systems, particularly when using automated image data analysis processes.[25] Based on the parameters specified for the sphere or cylinder, 3D Phantoms were generated and integrated on a 128 × 128 × 128 regular Cartesian grid with a resolution of 4.5 mm per pixel. Numerical integration was performed using the rectangle method, and each voxel was divided into 10^6 subvoxels.

Three phantoms were used in this study:

1. The NEMA SPECT Triple Line Source Phantom[27] consists of a water-filled cylinder with an inside diameter of 202 mm and a height of 200 mm, containing three axial line sources with a diameter of 1 mm.
2. The standard Jaszczak phantom with cold inserts[28] consists of a cylinder 186 mm high and 216 mm in diameter containing six spheres of diameters 12.7, 15.9, 19.1, 25.4, 31.8, and 38 mm, and 96 rods divided into 6 equal volumes based on their diameters of 6.4, 7.9, 9.5, 11.1, 12.7, or 19.1 mm (Figure 1).
3. The standard Jaszczak phantom with hot inserts features a background count per pixel equal to 10% of that of the hot insert (Fig.1).

These digital error-free phantoms consisted of 128 axial slices, represented the object to be imaged, and served as standard reference data for assessing the reconstructed slices.

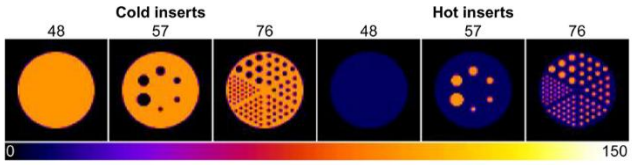

Figure 1: Transaxial Slices from Two Standard Jaszczak Phantoms This image depicts three sample images of transaxial slices from two standard Jaszczak phantoms. The phantom on the left contains cold inserts, while the one on the right includes hot inserts. The 48th slice is located in the uniform part of the phantom, the 57th slice is situated at the level of the plane containing the centers of the six phantom spheres, and the 76th transaxial slice is located at the level of the 96 rods. These 128x128 slices are displayed in 64x64 format, showing only the central part where the phantom appears.

B. Projection data simulation

Using a numerical phantom, we simulated ^{99m}Tc projections. The projection data modeled the acquisition of attenuated 140 keV photons with a parallel-hole collimator using a 128 × 128 matrix, 4.5 mm pixel size, 360◦ SPECT with 3˚ steps, and a 20 cm radius of rotation acquisition parameters. The simulation included attenuation, distance-dependent resolution, and Poisson noise. The Compton scatter effect was disregarded since this study aimed to assess the resolution recovery.

Knowing the position of the voxel M (x_M,y_M), the position of its projection M' (Fig. 2) on the detector is given by

$$k_{M'} = y_M \cos(\theta) - x_M \sin(\theta)$$

The three used phantoms were considered to be filled with water, both the containers and the hot or cold inserts. To simulate a ^{99m}Tc acquisition, the attenuation coefficient value (μ) for the narrow beam of 140 keV was assumed to be $0.15\ cm^{-1}$.

Voxel depth in the phantom is necessary to model attenuation. The phantom's cylindrical shape and known position allow for calculating the depth for a projection angle (Figure 2).

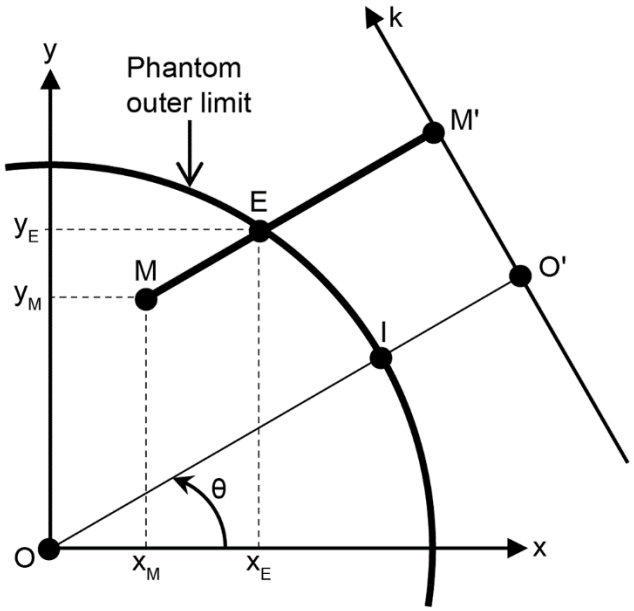

Figure 2: Modeling the Parallel-Projection Acquisition Geometry the k-axis represents the detector surface. Oxy: Represents the slice plane; Ok: Represents the detector surface; O: Indicates the slice center and cylindrical phantom center; OO': Denotes the detector radius of rotation; θ: Represents the projection angle; M: Represents the slice voxel center; M': Represents the projection of M on the detector; MM' or dD: Indicates the voxel–detector distance; OI or R: Represents the phantom radius; ME: Represents the voxel depth; and O'M' or kM': Represents the M' coordinate on the projection line.

Let $A = x_M \tan^2(\theta) - y_M \tan(\theta)$
$B = \sqrt{(R^2 - x_M^2)\tan^2(\theta) + 2\,x_M\,y_M \tan(\theta) - y_M^2 + R^2}$
$C = y_M - x_M \tan(\theta)$
the coordinates of point E(x_E, y_E) are:

$$x_E = \begin{cases} A + B, & -90^o < \theta < 90^o \\ A - B, & 90^o < \theta < 270^o \\ x_M, & \theta = -90^o \text{ or } 90^o \end{cases} \text{ and}$$

$$y_E = \begin{cases} x_E \tan(\theta) + C, & \theta \neq -90^o \text{ and } \theta \neq 90^o \\ \sqrt{R^2 - x_E^2}, & \theta = 90^o \\ -\sqrt{R^2 - x_E^2}, & \theta = -90^o \end{cases}$$

From which the depth ME is deduced:
$ME = \sqrt{(y_E^2 - y_M^2) + (x_E^2 - x_M^2)}$.
Metz's theoretical formulation was the foundation for the collimator-detector response model.[29] The collimator-detector's response function was approximated by a 2D Gaussian function, whose FWHM varies linearly with the distance (dD) from the source to the collimator.[30]
Clinical SPECT detectors usually provide an intrinsic spatial resolution for ^{99m}Tc in the 3–5 mm region. Nevertheless, the source-to-collimator distance and collimator design remarkably impact the SPECT system's image resolution. It generally falls within the 7–15 mm FWHM range for parallel-hole collimation of ^{99m}Tc and typical source-to-collimator distances.[19]

To replicate ideal conditions, the FWHM was varied from 7–15 mm for a distance (dD) ranging from 10–30 cm, covering the diameter of the phantom. This yields the simulation equation:
$FWHM(d_D) = 0.04\,d_D + 3$, where d_D and FWHM are expressed in mm.
The distance voxel detector (Fig. 2) is expressed as $dD = MM' = OO' - x_M \cos(\theta) - y_M \sin(\theta)$
The point spread function of the system was approximated using a two-dimensional Gaussian equation:

$$G(k,l) = \frac{4\ln(2)}{\pi\ FWHM^2}\ e^{-\left(\frac{4\ln(2)}{FWHM^2}\left((k-k_{M'})^2 + (l-l_{M'})^2\right)\right)}$$

where $M'(k_{M'}, l_{M'})$ is the voxel projection on the detector plane.
Simulations of noise-free and noisy projections were used. Five noisy projection sets were processed from each noise-free phantom's projection sets with total counts per projection of $2\ 10^6$, 10^6, $5\ 10^5$, $2.5\ 10^5$, and 10^5. These counts correspond to an average count/pixel in the Jaszczak phantom's projection area (1986 pixels) of approximately 1000, 500, 250, 125, and 50 (Table 1). These counts were chosen to be close to the real conditions and cover clinical and quality control applications.[24-26]

Poisson statistical noise was generated using these rescaled projection values. Suppose N is the noise-free projection pixel count. In that case, the noisy value must be an integer random number with a Poisson distribution of mean N. If the standard deviation for the Gaussian distribution is set equal to $\sqrt{N}$, the Gaussian and Poisson distributions look very similar once N exceeds ~ 20. N for all projections is greater than 20, except for a few pixels on the outer edge of the phantom;

therefore, the Gaussian distribution can be used.[31] In practice, the Delphi generator of random numbers with a Gaussian distribution of mean N and standard deviation $\sqrt{N}$ was used.
After generating the five noisy projections, their total count was rescaled to equal that of the non-noisy projection to facilitate the qualitative and quantitative comparison.

C. Resolution recovery and reconstruction procedure

This study used two projectors and back-projectors. The attenuation and distance-dependent response models were incorporated in the first projector (P1) exactly as described when constructing the projections (Paragraph B). P1 perfectly simulates the projections' acquisition. For the second projector (P2), the 2D Gaussian detector response was assumed to be independent of the source-detector distance. The average detector response was used with a FWHM of 10 mm. The attenuation process was incorporated into P2. P2 simulates an approximation of the projections' acquisition and is more easily implemented than P1.

The first back-projector (B1) is the transpose of P1 without attenuation modeling. The second (B2) is the transposition of P2 with a different FWHM of 7 mm and without attenuation modeling. We selected the FWHM to reduce the smoothing effect during the reconstruction and to accelerate the reconstruction convergence.[32] The images were reconstructed using MLEM with P1/B1, P1/B2, and P2/B2 as reconstruction pairs (Table 1).

Table 1: Procedures for the acquisition simulation and MLEM reconstruction pairs used in this study.

Projection simulation	P1{	FWHM (mm)	7 to 15 (10–30 cm from detector)																	
		mu (cm^{-1})	0.15																	
	C/p[a]		NF[b]			2x10^6			1x10^6			0.5x10^6			0.25x10^6			0.1x10^6		
Reconstruc-tion pair	Projector		P1	P1	P2	P1	P1	P2	P1	P1	P2	P1	P1	P2	P1	P1	P2	P1	P1	P2
	Back projector		B1	B2	B2	B1	B2	B2	B1	B2	B2	B1	B2	B2	B1	B2	B2	B1	B2	B2

P1: Projector incorporating attenuation correction and distance-dependent DRC. The collimator-detector response function was assumed to be a 2D Gaussian function, whose FWHM (7 to 15 mm) is linearly dependent on the source-detector distance. P2: Projector incorporating attenuation correction and distance-dependent DRC. The collimator-detector response function was assumed to be a 2D Gaussian function, whose FWHM (10 mm) is constant and equal to approximately the mean FWHM of the collimator-detector response. B1: Was the transpose of P1 without attenuation correction. B2: The transpose of P2 was done with an FWHM = 7mm and without attenuation correction. [a]: Counts/projection

D. Qualitative and quantitative assessment

To evaluate the qualitative and quantitative accuracy of the reconstruction methods, reconstructed transaxial slices of the Jaszczak phantom with cold and hot inserts were used.
Considering the reduced space occupied by the phantom in the 128 × 128 format slices, they have been displayed in a 64 × 64 format, retaining only the central part where the phantom appears.
Profile curves were used to evaluate the uniformity, noise, and edge artifacts qualitatively.
The root mean squared error (RMSE) between the reconstructed slices after i iterations $\left(\hat{T}^{(i)}\right)$ and the standard reference slices (T_S) was calculated as

$$RMSE = \sqrt{\frac{1}{N}\sum_{x=1}^{N}(\hat{T}^{(i)}(x) - T_s(x))^2}$$

where N is the total number of pixels inside the investigated region of the reconstructed slice.
The normalized mean error (NME) between the reconstructed slices after i iterations $(\hat{T}^{(i)})$ and the standard reference slices (T_S) was calculated as

$$NME = \frac{1}{N}\sum_{x=1}^{N}\left|(\hat{T}^{(i)}(x) - T_s(x))\right|$$

where N is the total number of pixels inside the investigated region of the reconstructed slice.
Jaszczak phantom spheres were used for the relative contrast (RC) measurement. The RC for each sphere was calculated by

$$RC = \frac{\frac{|C_S - C_B|}{C_B}}{\frac{|S_S - S_B|}{S_B}}$$

where C_S and S_S represent the sphere mean counts measured respectively on the reconstructed and standard reference slices. C_B and S_B represent the background mean counts measured respectively on the reconstructed and standard reference slices. The mean background counts are calculated in a spherical region of interest (ROI) located in the middle of the slices containing all the spheres and having the same size as the largest sphere.

The noise level can be assessed by the variance (dispersion of the data from the mean) in the uniform part of the phantom. For reconstructed transaxial slices, data can vary from the center to the border, even in the uniform part, especially during the first iterations. The variance can be higher and not be considered the true noise level representation. In this work, the average local variance (ALV) was selected to estimate the noise level.[33] ALV was calculated in a circular ROI of 13.5 cm (30 pixels) in diameter, drawn at the center of 3 transaxial slices in the uniform part of the Jaszczak phantom with cold inserts (from slice 47 to 49).
Each pixel of coordinates x and y in the ROI was considered the center of a 3 × 3 window. The local mean μ_{xy} for this pixel was calculated as follows:

$$\mu_{xy} = \frac{1}{9}\sum_{x'=-1}^{1}\sum_{y'=-1}^{1}\hat{T}^{(i)}(x + x', y + y')$$

where $\hat{T}^{(i)}$ is the reconstructed slice after i iterations and $\hat{T}^{(i)}(x, y)$ the pixel of coordinate x and y value.

The local variance LV_{xy} was calculated as

$$LV_{xy} = \frac{1}{9}\sum_{x'=-1}^{1}\sum_{y'=-1}^{1}(\hat{T}^{(i)}(x + x', y + y') - \mu_{xy})^2$$

The ROI average local variance was calculated as follows:

$$ALV = \frac{1}{N}\sum_{ROI} LV_{xy}$$

where N is the total number of pixels inside the ROI.

The FWHM of the line source images in an indicative sum of transaxial slices was used as the spatial resolution. To obtain the latter slice, 36 slices (from 46 to 81) reconstructed from the resolution phantom were added to minimize noise. An analysis tool that uses the method specified by the NEMA standard was developed for the calculations.[27]

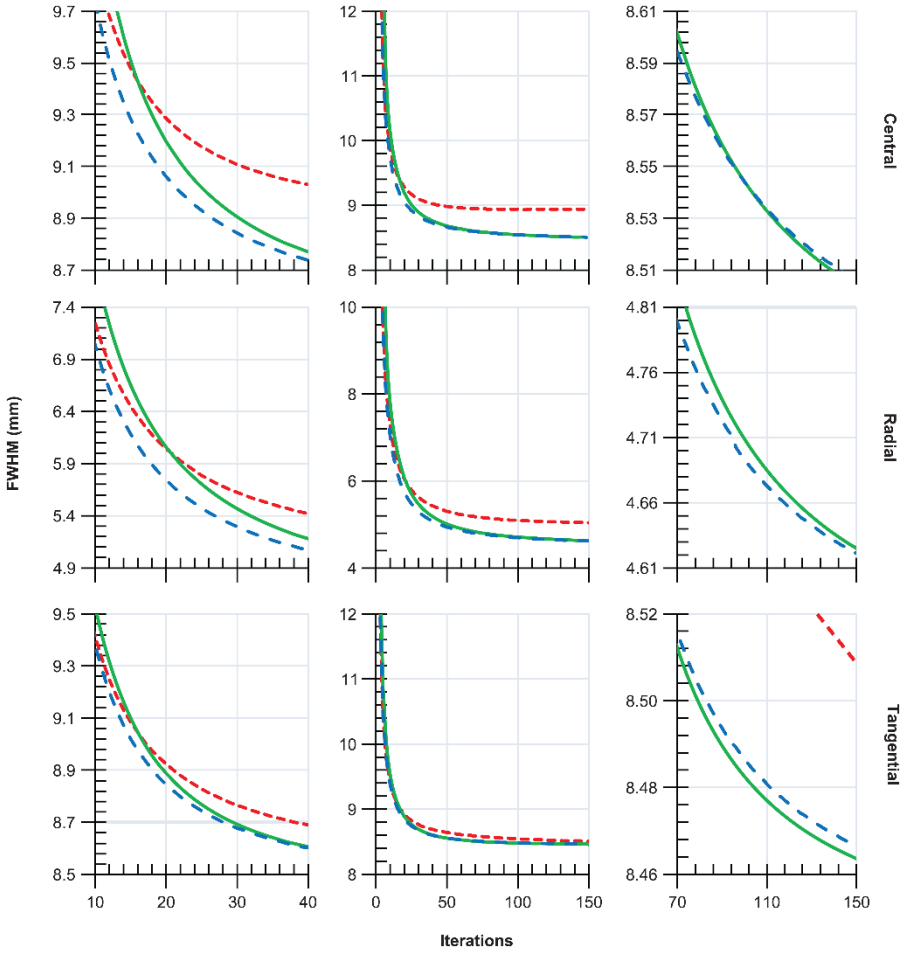

Figure 3: Full Width Half Maximum In this figure, we plot the full width at half maximum (FWHM) in the central, radial, and tangential directions against the iterative number. The FWHM values are obtained from the NEMA SPECT Triple Line Source Phantom. We utilize the MLEM reconstruction method with three different resolution compensation techniques. The first column depicts the initial iterations, and the second shows all and final iterations.

Results

The FWHM in the central, radial, and tangential directions was measured for all MLEM iterations using the NEMA SPECT Triple Line Source Phantom and the method specified by the NEMA standard.[27] The three resolution compensation methods investigated (Table 1) were compared. The results are shown in Fig. 3, which presents FWHM as a function of the iteration. The first, second, and third columns represent the first, overall, and last iteration results. At 150 iterations, the central, tangential, and radial resolutions reached ~8.5, 8.46, and 4.63 mm with both P1/B1 and P1/B2 (Table 2).

Table 2: Full Width Half Maximum (FWHM) Analysis

		FWHM (mm)								
		Central			Radial			Tangential		
Iteration		25	80	150	25	80	150	25	80	150
Method	P1/B1	9.02	8.58	8.50	5.70	4.78	4.63	8.77	8.50	8.46
	P1/B2	8.92	8.57	8.51	5.47	4.76	4.62	8.74	8.50	8.47
	P2/B2	9.17	8.94	8.94	5.79	5.14	5.04	8.83	8.57	8.51

Table 2 presents the Full Width Half Maximum (FWHM) values in the central, radial, and tangential directions for iterations 25, 80, and 150. FWHM was determined from the NEMA SPECT Triple Line Source Phantom. MLEM reconstruction was employed using the three investigated resolution compensation methods.

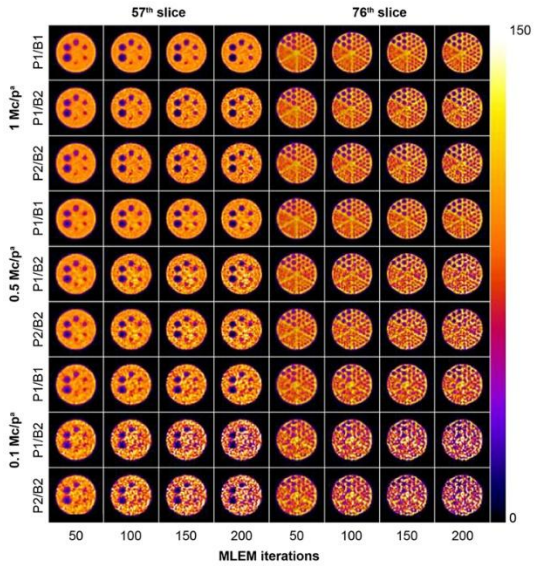

Figure 4: Reconstruction of 57th and 76th Transaxial Slices This figure presents the 57th and 76th reconstructed transaxial slices from the simulated projections, with 1, 0.5, and 0.1 Mcounts/projection, of the standard Jaszczak phantom with cold inserts. The reconstructions were performed using the three investigated resolution compensation methods: P1/B1, P1/B2, and P2/B2. These 128x128 slices are displayed in 64x64 format, focusing only on the central part where the phantom appears. [a]: 106 counts/projection

Figure 4 shows the 57th and 76th transaxial slices from the standard Jaszczak phantom with cold inserts. The 57th slice is located at the level of the plane containing the centers of the six phantom spheres. For all methods investigated, visual inspection shows that as iterations advance, contrast improves, but noise intensifies. In slices from the noisiest projections (low counts), distinguishing the smallest (e.g., 12.7 mm diameter) sphere is difficult. Edge artifacts also increase with iterations but are only noticeable in low-noise slices. Oscillation artifacts are also visible. Slices reconstructed using the reference method (P1/B1) were less noisy, but the edge artifacts were more intense than the other methods, confirmed by the profile curves (Fig. 5).

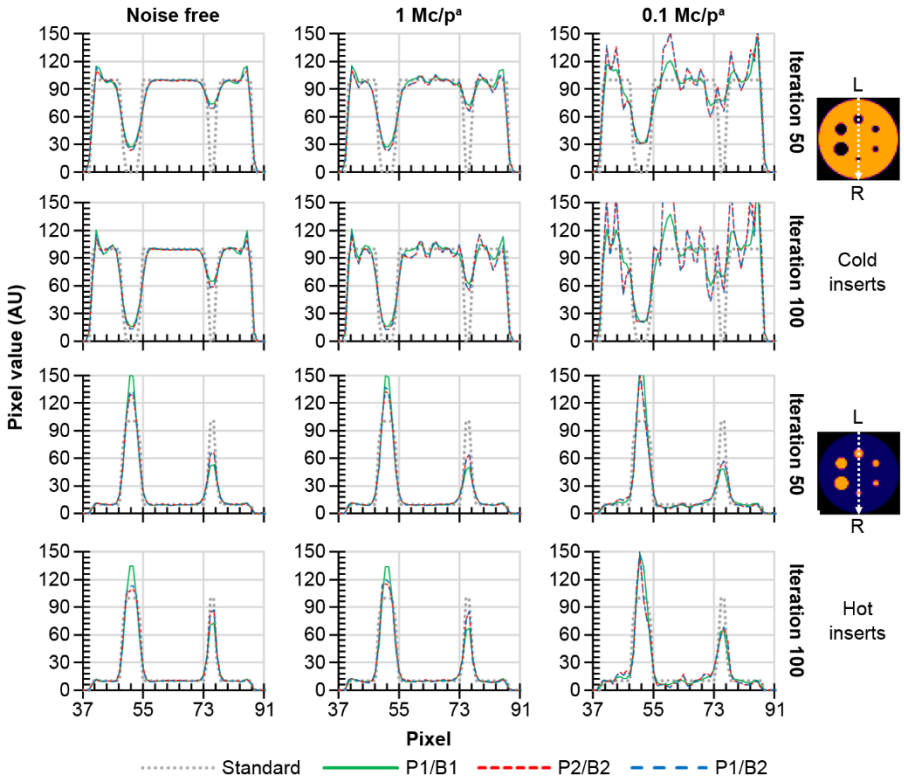

Figure 5. Comparison of Vertical Profiles This figure compares the vertical profiles through the center of the 57th reconstructed transaxial slices from simulated projections and noise-free data, at 1 Mcounts/projection and 0.25 Mcounts/projection, of the standard Jaszczak phantoms with cold and hot inserts. The reconstructions were performed using the three investigated resolution compensation methods P1/B1, P1/B2, and P2/B2. [a]: 106 counts/projection.

The 76th slice has 96 rods of diameters 6.4, 7.9, 9.5, 11.1, 12.7, and 19.1 mm. Rods that were 6.4 mm in diameter (lower than the minimum resolution of the detector) are invisible regardless of the noise level or reconstruction method used. The spatial resolution of the slices degrades as the noise level increases (from top to bottom). Additionally, contrast reduces from the edge to the center of the image. A similar observation was reported by Knoll P et al. for advanced iterative reconstruction methods.[34]

Figure 6 shows the 57th and 76th transaxial slices from the standard Jaszczak phantom with hot inserts. Compared to cold nodules (Fig. 4), the contrast and resolution of hot nodules were enhanced. The smallest sphere remains perceptible, and the contrast of the rods is more pronounced. Conversely, edge artifacts or overshooting appear on the large spheres, confirmed on the profile curves (Fig. 5).

The ALV values from the noise-free simulations are negligible compared to others, which are over 5000 times higher (Fig. 7, top–left). This indicates that image noise is mainly determined by Poisson noise in the simulated projection data, even for the highest counts per projection. The curves for P1/B2 and P2/B2 are very similar. Polynomial fits of order 2 for methods P1/B1 and P1/B2 show a high correlation with an R2 close to 1, indicating a parabolic trend of the ALV as a function of iterations. Using P1/B1 as a reconstruction pair reduced noise amplification compared to the other pairs.

Figure 8: Relative Contrast (RC) Analysis In this figure, we analyze the Relative Contrast (RC) as a function of the six sphere diameters of the standard Jaszczak phantoms with cold and hot inserts. We consider various iteration numbers noise levels and utilize the three investigated resolution compensation methods: P1/B1, P1/B2, and P2/B2. [a]: 106 counts/projection [b]: Noise-free projections

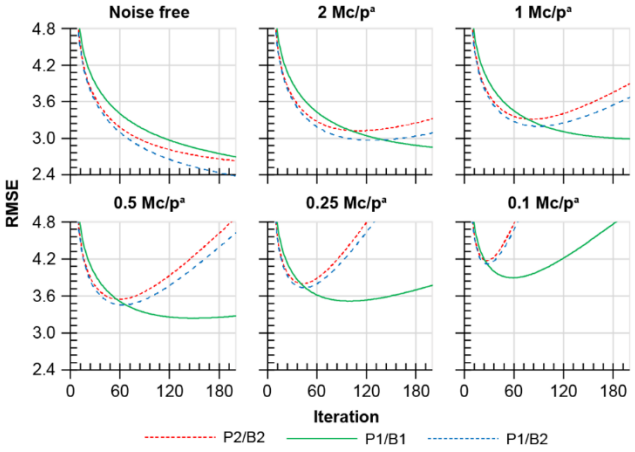

Figure 8 shows RC as a function of the six standard Jaszczak phantom sphere diameters for various iteration numbers, noise levels (3 columns), and the three resolution compensation methods (3 rows). Figure 8 includes cold and hot spherical inserts. Table 3 reports the RC values of cold and hot spherical inserts for various iteration numbers, noise levels, and the three resolution compensation methods. Contrast improves with increasing sphere size or iterations and is unrelated to noise level. The contrast of hot nodules is greater than that of cold nodules. Curves from no or low noise slices (left column) regularly increase, unlike those from noisy slices (right columns), which show irregularities accentuating with iterations. The P1/B2 reconstruction pair performs best, followed closely by P2/B2 (Table 3).

Table 3: Relative Contrast Comparison

Relative contrast														
Spheres diameter			12.7 mm						38 mm					
Counts/projection			1M			0.1M			1M			0.1M		
Iteration			50	100	150	50	100	150	50	100	150	50	100	150
Method	Cold inserts	P1/B1	0.30	0.40	0.46	0.29	0.38	0.43	0.71	0.80	0.83	0.69	0.77	0.81
		P1/B2	0.37	0.49	0.56	0.41	0.55	0.64	0.73	0.81	0.85	0.71	0.78	0.81
		P2/B2	0.36	0.48	0.55	0.41	0.55	0.64	0.73	0.81	0.84	0.71	0.78	0.81
	Hot inserts	P1/B1	0.47	0.60	0.67	0.43	0.54	0.59	0.94	0.92	0.92	0.94	0.91	0.92
		P1/B2	0.57	0.70	0.77	0.49	0.57	0.59	0.95	0.93	0.93	0.94	0.92	0.93
		P2/B2	0.56	0.69	0.76	0.48	0.56	0.59	0.93	0.91	0.92	0.92	0.91	0.92

Table 3 compares the relative contrast of two standard Jaszczak phantom spheres with cold and hot inserts across various iteration numbers and noise levels and the three investigated resolution compensation methods.

We calculated RMSE and NME for all reconstructed slices. Due to the similarities between RMSE and NME curves (distinguished only by the speed of convergence, which is higher for NME), Figure 9 only includes RMSE. The convergence iteration increases with counts per projection. Regardless of the noise level, P1/B1 is the slowest, and P1/B2 is the fastest. During the first iterations, the RMSE and NME of P1/B2 are lower than those of P1/B1 up to the point where the two curves intersect, after which P1/B1 takes over. The iteration corresponding to this intersection is reported in Fig. 10 and indicates the regions where methods P1/B1 and P1/B2 perform better regarding RMSE or NME. P1/B1 performs best for low counts and large iteration numbers, while P1/B2 is best for high counts and low iteration numbers.

Figure 10: Performance Comparison of Methods P1/B1 and P1/B2 This graph illustrates the regions where methods P1/B1 and P1/B2 perform better in terms of Root Mean Squared Errors (RMSE) or Normalized Mean Errors (NME). Method P1/B1 exhibits superior performance for low counts and large iteration numbers, while P1/B2 excels for high counts and low iteration numbers. The points represent the intersections of the RMSE (or NME) versus iteration curves of P1/B1 and P1/B2 for different counts (refer to Figure 9). Threshold lines are derived from second-order polynomial fitting.

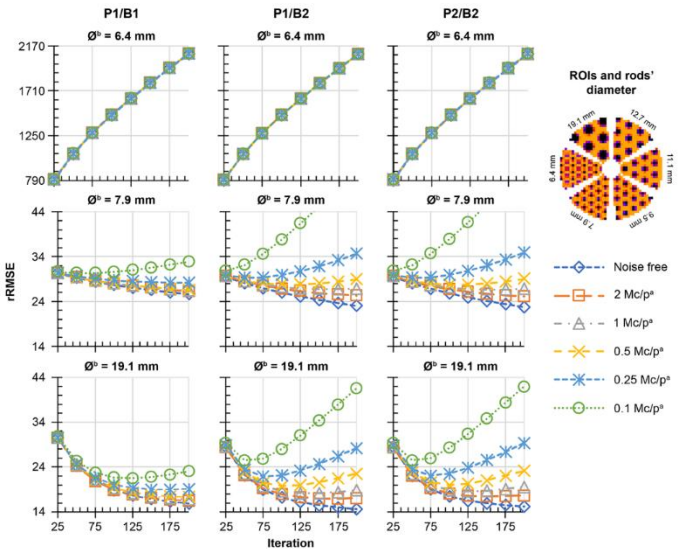

To study the reconstruction method's behaviors according to the size of the structures imaged, regional RMSEs (rRMSE) were calculated in 6 triangular ROIs, each including rods of the same diameter (Fig. 11). The results show different behaviors relative to the rods' diameters and noise levels. Curves for regions containing rods whose diameter was smaller than the resolution (6.4 mm) do not converge (Fig. 11, 1st line); in such cases, rRMSE values are much higher than in other regions. These curves occur independent of the projection noise level and reconstruction pair used. RRMSE in this region may be mainly due to the detector resolution limit, with noise making a negligible contribution. Except for this region, rRMSE decreases with the first iterations. For noise-free simulations, convergence is beyond the 200th iteration (the maximum in this work), regardless of the reconstruction pair or rods' diameter (Table 4). For low-noise simulations, convergence iteration (when < 200) decreases with the rods' diameter and increases for high-noise simulations (Table 4). The rRMSE convergence iteration is higher than the overall RMSE, except for the 7.9 mm rod's diameter region from the noisiest projections.

Table 4 displays the convergence iteration number and minimal rRMSE between the reconstructed axial slices and the calculated true phantom slices (reference) in the six triangular ROIs corresponding to the rods' region of the standard cold Jaszczak phantom. The data is presented for noise-free and noisy simulations. MLEM reconstruction was utilized with the three investigated resolution compensation methods.

Table 4: Convergence Iteration Number and Minimal rRMSE

Rods diameter			6.4 mm		7.9 mm		9.5 mm		11.1 mm		12.7 mm		19.1 mm		Overall	
Convergence It & rRMSE			It.	rRMSE	It.	rRMSE	It.	rRMSE	It.	rRMSE	It.	rRMSE	It.	rRMSE	It.	RMSE
Counts/projection and reconstruction pair	Noise Free	P1/B1	1	148	>200	25.6	>200	22.9	>200	19.1	>200	18.3	>200	15.9	>200	2.84
		P1/B2	1	163	>200	23.0	>200	19.4	>200	16.2	>200	16.5	>200	14.6	>200	2.53
		P2/B2	1	131	>200	22.7	>200	19.4	>200	16.6	>200	17.2	>200	15.2	>200	2.72
	2M	P1/B1	1	279	>200	26.2	>200	23.3	>200	19.5	>200	19.0	>200	16.4	>200	2.95
		P1/B2	1	177	>200	25.3	>200	21.7	197	19.0	171	19.6	170	17.0	127	2.97
		P2/B2	1	233	>200	25.1	>200	21.9	178	19.4	153	20.1	153	17.5	111	3.12
	1M	P1/B1	1	287	>200	26.4	>200	23.5	>200	19.6	>200	19.1	>200	16.8	>200	3.04
		P1/B2	1	189	165	26.7	184	23.6	158	20.1	143	20.2	137	18.1	89	3.20
		P2/B2	1	243	159	26.6	172	23.6	148	20.3	134	20.5	127	18.6	82	3.31
	0.5M	P1/B1	1	295	>200	26.5	>200	24.2	>200	21.1	>200	20.5	>200	17.4	150	3.24
		P1/B2	1	201	111	27.7	123	25.6	118	23.2	112	22.8	106	19.8	63	3.45
		P2/B2	1	252	110	27.7	118	25.6	109	23.4	108	23.0	101	20.0	59	3.55
	0,25M	P1/B1	1	303	>200	28.1	>200	26.2	>200	23.0	195	21.9	166	19.0	100	3.52
		P1/B2	1	212	58	29.2	80	28.3	73	25.9	82	25.3	82	21.9	44	3.73
		P2/B2	1	262	57	29.2	79	28.2	75	25.9	78	25.4	78	22.1	43	3.80
	0.1M	P1/B1	1	310	63	30.3	117	29.1	120	25.8	132	24.6	120	21.5	59	3.89
		P1/B2	1	223	14	30.6	41	30.7	46	28.4	57	28.1	59	25.3	28	4.12
		P2/B2	1	270	15	30.7	41	30.7	45	28.4	55	28.1	58	25.4	27	4.17

Discussion

On average, the spatial resolution improves with iteration (Fig. 3), and, surprisingly, the resolution of P1/B2 was approximated or exceeded P1/B1 for the central, radial, and tangential FWHMs and the 150 iterations (Table 2). In the digital transaxial slice, the ideal resolution varied from 1–2 pixels (4.5–9 mm) according to the position of the point source compared to the slice's pixels. If the position is at the center of the pixel, the resolution will be 1 pixel, and if it is at the intersection of 2 pixels, the resolution will be equal to 2 pixels. The three used sources were positioned according to the specifications of the NEMA SPECT Triple Line Source Phantom. For measurement of the central and tangential resolutions, the source was placed between 2 pixels; therefore, the ideal resolution should be close to 9 mm. Conversely, for the measurement of the radial resolution, the source was placed in the center of the pixel, and therefore, the ideal resolution should be very close to 4.5 mm. Taking these considerations into account, the correction of the resolution during the iterations becomes obvious.

The results show a parabolic growth of the reconstructed slices' ALVs (noise level) as a function of iterations. The two possible sources of error are Poisson noise and algorithmic noise. Since Poisson noise is absent in the noise-free set of simulations, the present noise in the corresponding reconstructed slices would be inherent to the algorithmic noise (Fig. 7, top-left). Table 5 demonstrates that Poisson noise ALV is almost inversely proportional to the total detected counts. Similar results were found by Liew et al. using Poisson noise variance.[35]

Table 5: Average Local Variance (ALV) per Count

		ALV × (C/p) × 10^{-6}								
Pairs		P1/B1			P1/B2			P2/B2		
C/p[a]		1M	0.5M	0.1M	1M	0.5M	0.1M	1M	0.5M	0.1M
Iteration	50	1.2	1.3	1.1	9.9	9.7	8.8	9.9	9.7	8.8
	100	4.2	4.4	4.0	36.4	35.9	33.6	36.8	36.3	33.9
	150	8.5	8.9	8.2	76.9	76.3	73.5	78.2	77.7	74.4
	200	14	14	14	130	130	128	133	132	130

Table 5 displays the Average Local Variance (ALV) multiplied by the counts per projection, scaled by 10^{-6}, for four iterations and three noisy simulations of the three studied reconstruction pairs. It demonstrates that ALV is nearly inversely proportional to the total detected counts. [a]: Counts per projection

It is known that MLEM allows for better resolution, a better signal-to-noise ratio, and better contrast compared to analytical methods. Nevertheless, MLEM presents two disadvantages that the iterations accentuate: noise amplification and edge artifacts. The images become noisier as successive estimates are generated with the MLEM algorithm. In addition, an abrupt change in intensity near the edges is accentuated and appears in successive estimates with overshoot accompanied by ringing, resembling the Gibb phenomenon.[36]

Edge artifacts generated during image reconstruction are related to the DRC. Strategies for managing these artifacts result in resolution deterioration.[32,37]

The edge artifact is only noticeable at high count levels. Otherwise, it would be dominated by the noise artifact (Fig. 4). From data of Fig. 5 (noise-free profile after 100 iterations), there were 20%, 15%, and 11% overshoots observed at the edges of the noise-free standard Jaszczak phantom reconstruction using P1/B1, P1/B2, and P2/B2 pairs, respectively These overshoots are less than those caused by noise in the same uniform part of the reconstruction of the noisy standard Jaszczak phantom. With small regions, this effect can show up as a visible dip at the center (Fig. 5, large sphere). Overshoots may occur with sufficiently small hot nodules where the edge artifacts start to merge (Figs. 5 and 6).

Figure 6. Reconstruction of 57th and 76th Transaxial Slices This figure presents the 57th and 76th reconstructed transaxial slices from simulated projections, with 1, 0.5, and 0.1 Mcounts/projection, of the standard Jaszczak phantom with hot inserts. The reconstructions were performed using the three investigated resolution compensation methods: P1/B1, P1/B2, and P2/B2. These 128x128 slices are displayed in 64x64 format, focusing only on the central part where the phantom appears. [a]: 106 counts/projection.

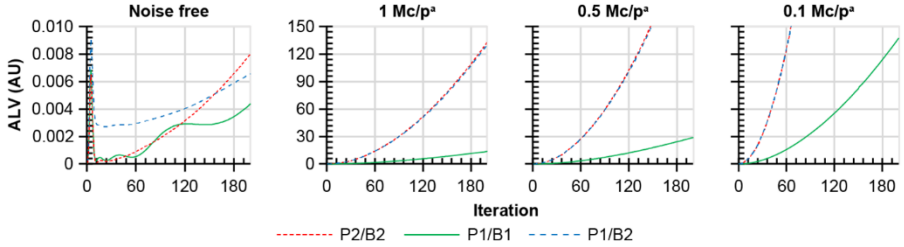

The curves of P1/B2 and P2/B2 (Fig. 7) are very close to each other and differ from P1/B1. The noise level relates more to the back-projector than the projector.

Figure 7: Average Local Variance (ALV) Analysis In this figure, we plot the Average Local Variance (ALV) as a function of the iteration number for noise-free and noisy simulations. We utilize MLEM reconstruction with the three investigated resolution compensation methods: P1/B1, P1/B2, and P2/B2. The ALV is calculated within a circular Region of Interest (ROI) with a diameter of 13.5 cm (30 pixels), drawn at the center of three transaxial slices in the uniform part of the Jaszczak phantom with cold inserts (see Figure 1), ranging from slices 47 to 49. For the methods P1/B1 and P1/B2, a polynomial fitting of order 2 is performed. The resulting R2 values are (0.9997, 0.9999), (0.9996, 0.9999), and (0.9998, 1) with 1, 0.5, and 0.1 Mcounts/projection, respectively. Trendlines have not been drawn to maintain the curves' visibility, illustrating the noise level's parabolic growth as a function of the iterations. [a]: 106 counts/projection.

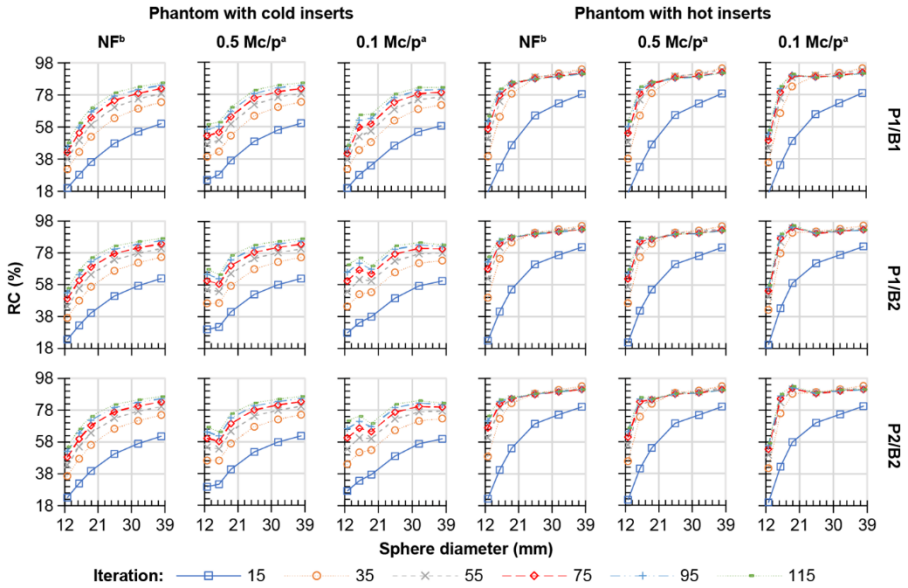

The RMSE measures the deviations between the reconstructed and supposedly ideal slices. RMSEs in this study relate mainly to the Poisson noise and the limited spatial resolution of the detector. As iterations progress, the spatial resolution improves on one side while the noise intensifies on the other. A compromise between the two is reached in the neighborhood of convergence (minimum RMSE). Poisson noise varies with counts per pixel, and the errors due to the resolution vary according to the size of the nodules in the phantom. Therefore, these deviations and their behavior with iterations can change according to the region where they are measured. The overall RMSE, as calculated, encompasses all voxels of the phantom. The regional rRMSE was calculated considering these variances. The results suggest that any structure with a size lower than the minimum resolution of the detector in terms of FWHM cannot be visualized.

Furthermore, this may indicate that in regions containing structures smaller than the resolution, an essential component of the rRMSE is caused by this limited resolution. This component can far outperform Poisson noise, resulting in rRMSE nonconvergence. This could explain why the convergence iteration in the five other regions is higher than the overall RMSE (Table 4). In addition to the noise level, the optimal number of iterations also depends on the region to be visualized and the size of the structures located there. Thus, the number of iterations should not seek an optimal resolution but a reasonable resolution related to the size of the structures sought and the level of the projections' noise. Searching for an optimal resolution will make structures larger than the resolution, noisier, and therefore less precise

Figure 9: Root Mean Squared Errors (RMSE) Analysis This figure illustrates the Root Mean Squared Errors (RMSE) between the 128 reconstructed axial slices and the 128 calculated true phantom slices (reference), plotted as a function of the iteration number for both noise-free and noisy simulations. We employ MLEM reconstruction with the three investigated resolution compensation methods: P1/B1, P1/B2, and P2/B2. [a]: 106 counts/projection

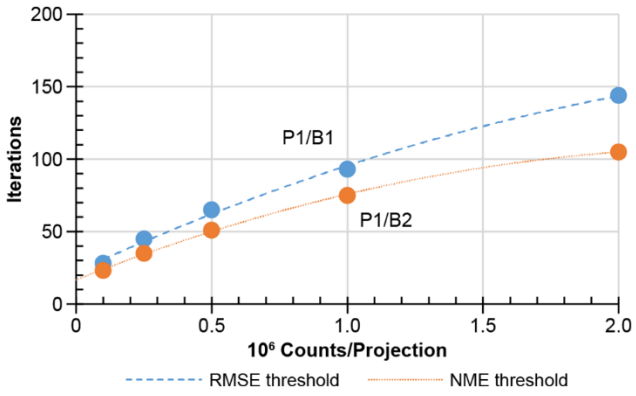

.

In Figs. 9 and 11, the curves obtained with P1/B2 decrease fastest and reach convergence earlier. Those obtained with P1/B1 have the slowest rate and reach convergence later but with the lowest error. The accelerated method results in enhanced numerical noise. This recalls the OSEM method, where a compromise between speedup (increasing the number of subsets) and image quality degradations (noise, artifacts) was necessary.[38]

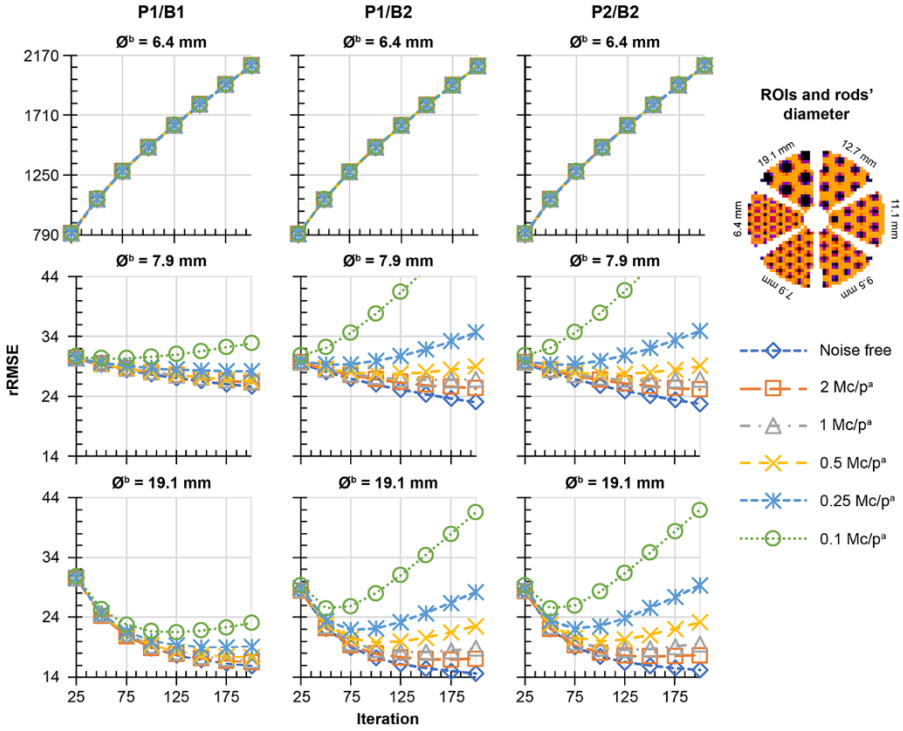

Figure 11: Regional Root Mean Squared Errors (rRMSE) Analysis This figure depicts the Regional Root Mean Squared Errors (rRMSE) between the reconstructed axial slices and the calculated true phantom slices (reference) in six triangular Regions of Interest (ROIs) corresponding to the rods' region of the standard Jaszczak phantom. The plot is presented as a function of the iteration number for noise-free and noisy simulations. MLEM reconstruction was employed using the three investigated resolution compensation methods. [a]: 106 counts/projection

The results confirm the superiority of P1 over P2 except for edge artifacts. They also highlight the importance of the back-projector choice. Using a less smoothing back-projector (lower FWHM) increases the speed of convergence, decreases edge artifacts, and improves contrast and spatial resolution but increases the noise level. At convergence, the RMSE (or NME) is higher.
This simulation did not include scatter. This represents an ideal situation in which the data had accurately compensated for the scatter. Consequently, the reconstructed slices would be qualitatively higher and more accurate than those obtained under normal conditions. Nevertheless, given that the purpose of this work was to study the DRC, this has no consequences on interpreting the results obtained.

The projection operator P1 was used during the simulation of the noise-free projections and in the tomographic reconstruction process. As previously mentioned, P1 represents the ideal projection operator for the distance-dependent DRC. Under real conditions, several factors may influence the projector accuracy, such as the detector response measurement errors, its Gaussian modeling approximations, or the linear dependence between the FWHM and source-detector distance. Thus, the results would be optimal and may represent the limit DRC can reach.

Even for well-performing reconstruction pairs, stopping iterations far from RMSE convergence (which in practice remains to be discovered) could lead to worse results than those obtained by less well-performing pairs. Therefore, the three pairs could be used. Although the performances of P2/B2 are globally inferior to P1/B2, they remain quite close. Its advantage is the simplicity of its implementation compared to the other methods. The number of iterations should be chosen according to the reconstruction pair, projection count, and desired spatial resolution.

Conclusions

None of the pairs investigated were more efficient than the others in terms of RMSE, NME, Relative Contrast, noise, or spatial resolution, and this depends on the projections' noise level, the phantom insert's size and type (cold or hot), and the considered iteration. In general, P1/B1 constitutes the most efficient reconstruction pair for low counts and large iteration numbers, and P1/B2 for high counts and low iteration numbers. P1/B1 appears to be the most effective against noise, whereas P1/B2 is the most effective for resolution compensation. Depending on the noise level of the projections and the number of iterations, the performance of P2/B2 is lower or very close to P1/B2. Its advantage is the simplicity of its implementation compared to the others.

List of Abbreviations

ALV	Average local variance
DRC	Detector-response compensation
MLEM	Maximum-likelihood expectation maximization
NME	Normalized mean error
PRF	Post-Reconstruction filtering
PSF	Point spread function
RC	Relative contrast
RMSE	Root mean squared error
ROI	Region of interest
SPECT	Single photon emission computed tomography

Declarations

Ethics approval and consent to participate

Not applicable.

Consent for publication

Not applicable.

Availability of data and materials

The datasets used and/or analysed during the current study are available from the corresponding author on reasonable request.

Competing interests

The authors declare that they have no competing interests.

Funding

This research did not receive any specific grant from funding agencies in the public, commercial, or not-for-profit sectors.

Authors' contributions

BZ and **NA** conceived and designed the analysis, collected the data, contributed data and analysis tools, performed the analysis, and were major contributors in writing the manuscript. **MA** performed the analysis and was a major contributor in writing the manuscript. All authors read and approved the final manuscript.

Acknowledgement

Not applicable.

References

1. Dewaraja YK, Schipper MJ, Roberson PL, Wilderman SJ, Amro H, Regan DD, et al. 131I-tositumomab radioimmunotherapy: initial tumor dose-response results using 3-dimensional dosimetry including radiobiologic modeling. J Nucl Med. 2010;51:1155-62. doi: 10.2967/jnumed.110.075176.
2. Sandström M, Garske U, Granberg D, Sundin A, Lundqvist H. Individualized dosimetry in patients undergoing therapy with (177)Lu-DOTA-D-Phe (1)-Tyr (3)-octreotate. Eur J Nucl Med Mol Imaging. 2010;37:212-25. doi: 10.1007/s00259-009-1216-8.
3. Dickson J, Ross J, Vöö S. Quantitative SPECT: the time is now. EJNMMI Phys. 2019;6:4. doi: 10.1186/s40658-019-0241-3.
4. Jaszczak RJ, Coleman RE, Whitehead FR. Physical factors affecting quantitative measurements using camera-based single photon emission computed tomography (Spect). IEEE Trans Nucl Sci. 1981;28:69-80. doi: 10.1109/TNS.1981.4331143.
5. Marquis H, Deidda D, Gillman A, Willowson KP, Gholami Y, Hioki T, et al. Theranostic SPECT reconstruction for improved resolution: application to radionuclide therapy dosimetry. EJNMMI Phys. 2021;8:16. doi: 10.1186/s40658-021-00362-x.
6. Sorenson JA, Phelps ME. Physics in nuclear medicine second edition. New York: Grune & Stratton Inc; 1987.
7. Anger HO. Scintillation camera with multichannel collimators. J Nucl Med. 1964;5:515-31.

8. Tsui BMW, Zhao XD, Frey EC, Ju Z-W, Gullberg GT. Characteristics of reconstructed point response in three-dimensional spatially variant detector response compensation in SPECT. In: Grangeat P, Amans J-L, editors. Three-dimensional image reconstruction in radiology and nuclear medicine. Berlin: Springer Netherlands; 1996. p. 149-61. doi: doi.org/10.1007/978-94-015-8749-5_11
9. Seret A, Nguyen D, Bernard C. Quantitative capabilities of four state-of-the-art SPECT-CT cameras. EJNMMI Res. 2012;2:45. doi: 10.1186/2191-219X-2-45.
10. King MA, Schwinger RB, Doherty PW, Penney BC. Two-dimensional filtering of SPECT images using the Metz and Wiener filters. J Nucl Med. 1984;25:1234-40.
11. Lewitt RM, Edholm PR, Xia W. Fourier method for correction of depth-dependent collimator blurring. J Med Imaging. 1989;1092:III.
12. Glick SJ, Penney BC, King MA, Byrne CL. Noniterative compensation for the distance-dependent detector response and photon attenuation in SPECT imaging. IEEE Trans Med Imaging. 1994;13:363-74. doi: 10.1109/42.293929.
13. Hawkins WG, Leichner PK. An intrinsic 3D Wiener filter for the deconvolution of spatially varying collimator blur. In: Proceedings of 1st International Conference on Image Processing; vol 2; 1994. p. 163-7.
14. Floyd CE, Jaszczak RJ, Manglos SH, Coleman RE. Compensation for collimator divergence in SPECT using inverse Monte Carlo reconstruction. IEEE Trans Nucl Sci. 1988;35:784-7. doi: 10.1109/23.12832.
15. Tsui BMW, Hu HB, Gilland DR, Gullberg GT. Implementation of simultaneous attenuation and detector response correction in SPECT. IEEE Trans Nucl Sci. 1988;35:778-83.
16. Formiconi AR, Pupi A, Passeri A. Compensation of spatial system response in SPECT with conjugate gradient reconstruction technique. Phys Med Biol. 1989;34:69-84. doi: 10.1088/0031-9155/34/1/007.
17. McCarthy AW, Miller MI. Maximum likelihood SPECT in clinical computation times using mesh-connected parallel computers. IEEE Trans Med Imaging. 1991;10:426-36. doi: 10.1109/42.97593.
18. Miller MI, Butler CS. 3-D maximum a posteriori estimation for single photon emission computed tomography on massively parallel computers. IEEE Trans Med Imaging. 1993;12:560-5. doi: 10.1109/42.241884.
19. Ritt P, Vija H, Hornegger J, Kuwert T. Absolute quantification in SPECT. Eur J Nucl Med Mol Imaging. 2011;38(suppl 1):S69-S77. doi: 10.1007/s00259-011-1770-8.
20. Shepp LA, Vardi Y. Maximum likelihood reconstruction for emission tomography. IEEE Trans Med Imaging. 1982;1:113-22. doi: 10.1109/TMI.1982.4307558.
21. Lange K, Carson R. EM reconstruction algorithms for emission and transmission tomography. J Comput Assist Tomogr. 1984;8:306-16.
22. Hutton BF, Lau YH. Application of distance-dependent resolution compensation and post-reconstruction filtering for myocardial SPECT. Phys Med Biol. 1998;43:1679-93. doi: 10.1088/0031-9155/43/6/022.
23. Tsui BM, Frey EC, Zhao X, Lalush DS, Johnston RE, McCartney WH. The importance and implementation of accurate 3D compensation methods for quantitative SPECT. Phys Med Biol. 1994;39:509-30. doi: 10.1088/0031-9155/39/3/015.
24. Kapucu OL, Nobili F, Varrone A, et al. EANM procedure guideline for brain perfusion SPECT using 99mTc-labelled radiopharmaceuticals, version 2. Eur J Nucl Med Mol Imaging. 2009;36:2093-102. doi: 10.1007/s00259-009-1266-y.

25. Hirtl A, Bergmann H, Knäusl B, Beyer T, Figl M, Hummel J [technical note]. Technical Note: Fully-automated analysis of Jaszczak phantom measurements as part of routine SPECT quality control. Med Phys. 2017;44:1638-45. doi: 10.1002/mp.12150.
26. Dorbala S, Ananthasubramaniam K, Armstrong IS, Chareonthaitawee P, DePuey EG, Einstein AJ, et al. Single photon emission computed tomography (SPECT) myocardial perfusion imaging guidelines: instrumentation, acquisition, processing, and interpretation. J Nucl Cardiol. 2018;25:1784-846. doi: 10.1007/s12350-018-1283-y.
27. Association NEM. NEMA standards publication NU 1-2007: performance measurements of gamma cameras. Rosslyn: National Electrical Manufacturers Association; 2007.
28. CSPMedical. Standard Jaszczak phantom. 2023. https://cspmedical.com/jaszczak-spect-phantom/. Accessed 14 Feb 2023.
29. Metz CE, Atkins FB, Beck RN. The geometric transfer function component for scintillation camera collimators with straight parallel holes. Phys Med Biol. 1980;25:1059-70. doi: 10.1088/0031-9155/25/6/003.
30. Yokoi T, Shinohara H, Onishi H. Performance evaluation of OSEM reconstruction algorithm incorporating three-dimensional distance-dependent resolution compensation for brain SPECT: A simulation study. Ann Nucl Med. 2002;16:11-8. doi: 10.1007/BF02995286.
31. Rzeszotarski MS. The AAPM/RSNA physics tutorial for residents. RadioGraphics. 1999;19:765-82. doi: 10.1148/radiographics.19.3.g99ma33765.
32. Rahmim A, Qi J, Sossi V. Resolution modeling in PET imaging: theory, practice, benefits, and pitfalls. Med Phys. 2013;40:064301. doi: 10.1118/1.4800806.
33. Woodcock CE, Strahler AH. The factor of scale in remote sensing. Remote Sens Environ. 1987;21:311-32. doi: 10.1016/0034-4257(87)90015-0.
34. Knoll P, Kotalova D, Köchle G, Kuzelka I, Minear G, Mirzaei S, et al. Comparison of advanced iterative reconstruction methods for SPECT/CT. Z Med Phys. 2012;22:58-69. doi: 10.1016/j.zemedi.2011.04.007.
35. Liew SC, Hasegawa BH, Brown JK, Lang TF. Noise propagation in SPECT images reconstructed using an iterative maximum-likelihood algorithm. Phys Med Biol. 1993;38:1713-26. doi: 10.1088/0031-9155/38/12/003.
36. Snyder DL, Miller MI, Thomas LJ, Politte DG. Noise and edge artifacts in maximum-likelihood reconstructions for emission tomography. IEEE Trans Med Imaging. 1987;6:228-38. doi: 10.1109/TMI.1987.4307831.
37. Watson CC. Estimating effective model kernel widths for PSF reconstruction in PET. In 2011 IEEE Nuclear Science Symposium Conference Record, IEEE; 2011. p. 2368-74.
38. Morey AM, Kadrmas DJ. Effect of varying number of OSEM subsets on PET lesion detectability. J Nucl Med Technol. 2013;41:268-73. doi: 10.2967/jnmt.113.131904.